Atmospheric
Chemistry
and Physics

Discussions

Open Access

1

2

The influence of particle composition upon

the evolution of urban ultrafine diesel

particles on the neighbourhood scale

6

7

Irina Nikolova[1], Xiaoming Cai[1], Mohammed Salim Alam[1],

Soheil Zeraati-Rezaei[2], Jian Zhong[1], A. Rob MacKenzie[1,3*]

and Roy M. Harrison[1,4]

11

12

[1]School of Geography, Earth and Environmental Sciences

University of Birmingham, Edgbaston, Birmingham B15 2TT

United Kingdom

16

[2]Department of Mechanical Engineering

Atmospheric
Chemistry
and Physics
Discussions

Open Access

EGU

18   **University of Birmingham, Edgbaston, Birmingham B15 2TT**

19   **United Kingdom**

20

21   **[3]Birmingham Institute of Forest Research (BIFoR)**

22   **University of Birmingham, Edgbaston, Birmingham B15 2TT**

23   **United Kingdom**

24

25   **[4]Also at: Department of Environmental Sciences / Center of**

26   **Excellence in Environmental Studies, King Abdulaziz University, PO**

27   **Box 80203, Jeddah, 21589, Saudi Arabia**

28

29   **[*]Corresponding author: a.r.mackenzie@bham.ac.uk**

30

31

32

33

34

35

36

37

38

39

40

Atmospheric
Chemistry
and Physics
Discussions

41

42 **ABSTRACT**

43 A recent study demonstrated that diesel particles in urban air undergo evaporative shrinkage

44 when advected to a cleaner atmosphere (Harrison et al., 2016,). We explore, in a structured and

45 systematic way, the sensitivity of nucleation-mode diesel particles to changes in particle

46 composition and saturation vapour pressure. We use a multi-component aerosol microphysics

47 model based on surrogate molecule (C_{16}-C_{32} n-alkane) volatilities. For standard atmospheric

48 conditions (298 K, 1013.25hPa), and over timescales (ca. 100 s) relevant for dispersion on the

49 neighbourhood scale (up to 1 km), the choice of a particular vapour pressure dataset changes the

50 range of compounds that are appreciably volatile by 2-6 carbon numbers. The nucleation-mode

51 peak diameter, after 100 s of model runtime, is sensitive to the vapour pressure parameterisations

52 for particles with compositions centred on surrogate molecules between $C_{22}H_{46}$ and $C_{24}H_{50}$. The

53 vapour pressures of components in this range are therefore critical for the modelling of

54 nucleation-mode aerosol dynamics on the neighbourhood scale and need to be better constrained.

55 Laboratory studies have shown this carbon number fraction to derive predominantly from engine

56 lubricating oil. The accuracy of vapour pressure data for other (more and less volatile)

57 components from laboratory experiments, is less critical. The influence of a core of involatile

58 material is also considered.

59

60 The new findings of this study may also be used to identify the Semi-Volatile Organic Compound

61 (SVOC) compositions that play dominating roles in the evaporative shrinkage of the nucleation

62 mode observed in field measurements (e.g. Dall'Osto et al., 2011). As well as reconciling model

63 and observations, identifying the most significant vapour pressure regime for nucleation-mode

64 dynamics offers a way to improve the computing efficiency of urban aerosol models by adopting

65 simplified schemes for those less important components: e.g., an equilibrium scheme for low-

66 carbon-number components and a linear scheme for high-carbon-number components.

1.   INTRODUCTION

67

68 Ultrafine particles (UFP, with particle diameter Dp < 100 nm) have been increasingly a focus of

69 urban air research over the last two decades. The main source of UFP in outdoor urban air is

70 typically road traffic (Kumar et al., 2014). Harrison et al. (2011) reported that on a busy highway

71 in central London, UK, 71.9% of particles by number were traffic-generated; of which 27.4% are

72 found in the semi-volatile exhaust nucleation mode, 38% are in the exhaust solid mode and the

73 remaining 6.5% are from brake dust and resuspension (Harrison et al., 2011). The proximity of

74 the UFP traffic source to the public, and the large number of UFP emitted by traffic, have

75 prompted health-related research that has accrued evidence pointing to the toxicity and

76 potentially harmful effects of UFP on human health (Atkinson et al., 2010). Experimental and

77 modelling studies have advanced our understanding of the behaviour of urban air UFP, e.g. the

78 relevant aerosol dynamics important to the evolution of the UFP in space and time (Allen et al.,

79 2007; Biswas et al., 2007; Dall'Osto et al., 2011; Nikolova et al., 2011; Karnezi et al, 2014).

80

81 Nonetheless, key information regarding the size-resolved composition of the UFP is missing,

82 which limits our ability to determine the impact of gas-transfer processes on UFP evolution.

83 Progress has been made in identifying the composition of traffic-generated particles (including

84 the ultrafine fraction) by resolving the so-called 'unresolved complex mixture' (largely

85 uncharacterised organics in traditional gas chromatography) via two-dimensional gas

86 chromatography (GC×GC; Chan et al., 2013). Alam et al. (2016) show that emitted ultrafine

87 diesel particles consist of a substantial amount of organic material from both unburnt

88 diesel fuel and engine lubricating oil. They attribute the low molecular weight Semi-Volatile

89 Organic Compounds (SVOCs, having carbon number < 18) predominantly to the unburnt diesel

90 fuel, whereas heavier SVOCs (carbon number > 18) are attributed predominantly to the engine

91 lubricating oil. A typical GC×GC separation is shown in the chromatogram (Figure 1) for diesel

92 engine exhaust emissions in the particulate-phase Aitken mode ($56 < D_p < 100$ nm). Compounds

Atmospheric
Chemistry
and Physics
Discussions

93   are separated by volatility along the *x*-axis (first separation dimension) and by polarity in the *y*-

94   axis (second dimension). Peak identification is based on retention indices and mass spectral data

95   from the National Institute of Standards and Technology (NIST) library. The majority of

96   chromatography peaks (identified as aliphatic alkanes, lower black polygons) are present between

97   C_{18} to C_{26}, corresponding to the compounds identified in the engine lubricating oil and particulate

98   phase engine emissions (Alam et al. 2017). Bar charts above the chromatogram show the

99   volatility distribution of total alkanes (red) and total identified compounds (black), indicating

100   that, although many hundreds of individual chemical compounds are detected, the majority of the

101   SVOCs emissions consist of alkanes. Both the alkane composition and the total composition

102   distributions show a broad peak centred at C_{25}.

103

104   Most primary organic particle emissions are semi-volatile in nature and thus they are likely to

105   evaporate with atmospheric dilution and moving away from the source (Robinson et al., 2007).

106   This has been observed by Dall'Osto et al. (2011; see also Figure 1- S in Supplementary

107   Information) as part of the REPARTEE campaign (Harrison et al., 2012). Dall'Osto et al. (2011)

108   reported a remarkable decrease in the measured nucleation-mode peak particle diameter ($D_{pg,nuc}$)

109   between a street canyon ($D_{pg,nuc}$ = 23 nm) and the downwind neighbourhood ($D_{pg,nuc}$ = 8-9 nm) ca.

110   650 m distant in central London (UK). Nucleation formation of new particles in the atmosphere

111   was ruled out as a possible reason for the observed behaviour. Instead, the decrease in particle

112   diameter was attributed to the effect of evaporation and substantial mass loss from the particle

113   surface (hereafter referred to as REPARTEE-like aerosol dynamics). Alam et al. (2016) present

114   the composition of diesel UFP particles measured on a laboratory test-rig (cf. Figure 2-S in

115   Supplementary Information), however the range of variability of the particle composition in

116   emissions is still unknown. It is also not known how the organic material is distributed onto the

117   nucleation and Aitken modes of the UFP distribution in the atmosphere.

118

Atmospheric
Chemistry
and Physics
Discussions

119   Numerical experiments can test the plausibility of possible missing components of the system,

120   and can advise on which experimental studies will be most likely to resolve the existing

121   knowledge gaps. Nikolova et al. (2016) describe a modelling framework that can produce

122   nucleation-mode dynamics consistent with observations. However, missing in that study is the

123   identification of critical thermodynamic parameters and size-resolved composition that could

124   determine or point to a REPARTEE-like aerosol dynamics.

125

126   In the present study, we develop a method to search the particle composition space — i.e. the

127   volatility parameter space — to identify a group of surrogate n-alkanes in the $C_{16}H_{34}$-$C_{32}H_{66}$ range

128   that could explain a decrease in the nucleation-mode particle diameter to 10 nm or below as seen

129   in the measurements in London (Dall'Osto et al., 2011). We provide a more robust approach to

130   identify crucial parameters responsible for the UFP behaviour in the atmosphere on the

131   neighbourhood scale including the identification of parameter sets that are incompatible with the

132   observed behaviour in urban air of nucleation mode UFP. We describe a new way to simulate and

133   evaluate the role of the SVOCs composition on the atmospheric behaviour of the size-resolved

134   urban UFP and examine more complex sets of composition involving a non-volatile core. We also

135   assess the critical role of saturation vapour pressure on the size-resolved aerosol dynamics.

136

137   In this study we use Lagrangian box-model simulations of the evolution of urban ultrafine diesel

138   particles on the neighbourhood scale (up to 1 km). Key results will be presented and discussed in

139   the main text; more details are provided in the Supplementary Information. The Methodology

140   section describes the modelling approach. The Results section presents the model output. In the

141   Discussion and Conclusions sections, the key findings are summarised with suggestions for

142   further work.

143

144   **2.   METHODOLOGY**

Atmospheric
Chemistry
and Physics
Discussions

Open Access

145   We adopt a 'surrogate molecule' approach to UFP composition, based on the chemical speciation

146   shown in analyses such as Figure 1. The composition of UFP is simulated as comprising n-

147   alkanes from $C_{16}H_{34}$ to $C_{32}H_{66}$, which are the most abundant compounds in Figure 1. Previously

148   (Nikolova et al., 2016), we initialised the n-alkane abundance in gas and particle phases using

149   roadside and urban background observations in Birmingham, U.K. (Harrad et al., 2003). In what

150   follows, we retain this roadside gas-phase initialisation (see below), but choose a more general

151   method for initialising the particle composition, in order to test the sensitivity of the results to the

152   initialisation in a systematic way. By adopting a surrogate molecule approach, we are effectively

153   anchoring the model volatility basis set in physico-chemical data, as discussed further below.

154

155   The SVOC mass fractions in a particle are represented by a truncated Gaussian distribution that is

156   centred for each model run at a given n-alkane in the range from $C_{16}H_{34}$ to $C_{32}H_{66}$ with a standard

157   deviation, σ, varying from 1 to 5. Below we call the surrogate n-alkane on which the composition

158   distribution is centred, the *modal composition*. Example compositions are shown in Figure 2 for a

159   Gaussian distribution centred at $C_{24}H_{50}$. A narrower mass distribution, with $\sigma = 1$, focuses

160   predominantly (ca. 40%) on the component, j ($C_{24}H_{50}$), at which the distribution is centred, with a

161   smaller (ca. 24%) contribution from the adjacent compounds $C_{23}H_{48}$ and $C_{25}H_{52}$, and a minor

162   contribution (ca. 5%) from $C_{22}H_{46}$ and $C_{26}H_{54}$. The contribution of the remaining compounds from

163   the tail of the distribution is very low and less than 1%. However, a wider mass distribution (e.g.

164   $\sigma = 5$) approximates a flat distribution and includes a contribution from the majority or all of the

165   compounds in the n-alkane range $C_{16}H_{34}$-$C_{32}H_{66}$. Monotonically decreasing distributions occur for

166   distributions centred at either end of the $C_{16}H_{34}$-$C_{32}H_{66}$ range. Overall, if one excludes the

167   compounds with less than 1% contribution, modal compositions centred at carbon number, j, with

168   $\sigma = 1, 2, 3, 4, \& 5$, contain surrogate compounds +/- 2, 4, 7, 9, and 11 carbon numbers of j

169   (formally, to remain in the 16-32 carbon number range, [max(16, j-2):min(32, j+2)], [max(16, j-

170   4):min(32, j+4)], [max(16, j-7):min(32, j+7], [max(16, j-9):min(32, j+9], & [max(16, j-

Atmospheric
Chemistry
and Physics
Discussions

171 11):min(32, j+11)]).

172

173 We use a Gaussian distribution to represent the composition of the particles because it provides a

174 structured and systematic way to evaluate the organic-aerosol phase partitioning and the amount

175 of organic matter in the UFP. This is important for the behaviour and evolution of the UFP at

176 various timescales relevant for the urban atmosphere. Although there is no reason to discount

177 other functional forms for the composition distribution (e.g., skew Gaussian, log-normal, Pareto,

178 linear, etc), the Gaussian distributions chosen represent a simple two-parameter approach to

179 explore the volatility/composition space available.

180

181 **2.1   Box Model**

182 The model used in this study is the UFP version (Nikolova et al., 2016) of CiTTy-Street (Pugh et

183 al., 2012); that is, a box-model configuration that accounts for the multicomponent nature of the

184 urban ultrafine particles. The CiTTy-Street-UFP model is used with 15 discrete size bins, with an

185 initial diameter range between 5.8-578 nm in a uniform log-scale. The model can operate in two

186 modes with respect to the aerosol dynamics: Eulerian (fixed particle-diameter grid) or Lagrangian

187 (moving particle-diameter grid). The Eulerian mode is selected when the UFP size distribution is

188 evaluated in the presence of emissions and exchange of particles between boxes (Nikolova et al.,

189 2016). The Lagrangian mode can be selected when the UFP size distribution is evaluated for an

190 isolated air parcel, i.e., when no emissions or transport between boxes are present. In this study,

191 the Lagrangian mode is selected in a zero-dimensional configuration with no emissions or

192 transport in/out of the box. The UFP dynamics (only condensation/evaporation) are simulated

193 such that particles are allowed to grow/shrink to their exact size without any redistribution onto

194 fixed bins in a grid with bin bounds left open in a fully moving diameter scheme (see, for

195 example, Jacobson et al., 1997). The condensation/evaporation process accounts for Raoult's

196 Law, the Kelvin effect, and a mass accommodation coefficient $\alpha = 1$ (Julin et al., 2014) for all

197 components. The model results are evaluated at 1, 10 and 100 s. The timescale of 100 s is based

198 on estimate of the travel time on the neighbourhood scale (i.e., horizontal travel distances << 1

199 km).

2.2   Modal Composition and Initial Size-Resolved UFP distribution

201 The initial size-resolved UFP distribution is based on the measurements of Dall'Osto et al. (2011)

202 and reproduced in Figure 1-S in the Supplementary Information. This ultrafine size distribution

203 represents the typical street canyon bimodal size distribution found next to a traffic site, e.g. next

204 to Marylebone Road in London (UK). The distribution has a well-defined nucleation mode with a

205 peak number concentration at $D_{pg,nuc}$ ~ 23-24 nm. The Aitken mode appears as a shoulder attached

206 to the nucleation mode with a peak number concentration found at $D_{pg,aim}$ between 50-60 nm.

207 The initial UFP size-resolved composition is represented by modal compositions in the range

208 $C_{16}H_{34}$-$C_{32}H_{66}$, as detailed above, and a standard deviation σ from 1 to 5. A non-volatile core is

209 included in the ultrafine particles. While studies broadly agree on the existence of a non-volatile

210 core in the Aitken mode (Biswas et al., 2007; Wehner et al., 2004; Ronkko et al., 2013), it is

211 unclear if nucleation-mode particles contain some non-volatile material or if they are entirely

212 composed of (semi-)volatile SVOC. We have tested the sensitivity to the existence of non-volatile

213 material in the nucleation mode particles by initialising with 1%, 5% or 10% by mass non-

214 volatile material for each modal composition (see Supplementary Information for details of the

215 initialisation); results are discussed later in this paper. Simulations are performed by considering

216 the initialised Aitken mode predominantly non-volatile and coated only with 10% volatile

217 material. This is based on the observations during the REPARTEE campaign (Harrison et al.,

218 2012) that show a fairly stable Aitken mode between the street canyon and the neighbourhood.

219 The initial size-resolved modal compositions, composition standard deviations and non-volatile

220 core in the nucleation and Aitken modes are detailed in Tables 1-S, 2-S, 3-S and 4-S in the

221 Supplementary Information. We also provide information on the input parameters of the log-

222 normal UFP size distribution for Nucleation and Aitken modes.

223

2.3 Saturation Vapour Pressures and Gas-Phase Concentrations

225 The driving force for condensation/evaporation is the difference between the partial pressure of

226 each representative SVOC and its saturation vapour pressure (hereafter vapour pressure) over the

227 ideal solution in the nucleation mode condensed phase. Figure 3 shows vapour pressures above

228 pure, flat, supercooled liquids for n-alkanes in the range $C_{16}H_{34}$-$C_{32}H_{66}$, following Chickos and

229 Lipkind (2008), Compernolle et al. (2011), the Epi Suite calculator (US EPA, 2017), and the

230 UmanSysProp tool (Topping et al., 2016). The UmanSysProp tool provides vapour pressure data

231 based on the work of Nannoolal et al. (2008) and Myrdal and Yalkowsky (1997) with the boiling

232 points of Joback and Reid (1987), Stein and Brown (1994), and Nannoolal et al. (2004). There is

233 a very substantial range of estimated vapour pressures for the same compounds in Figure 3,

234 especially for the high molecular weight n-alkanes. The reported data agrees within an order of

235 magnitude between $C_{16}H_{34}$ and $C_{19}H_{40}$, but discrepancies of much more than an order of

236 magnitude are evident for the high molecular weight compounds. An enormous difference in the

237 vapour pressure for $C_{32}H_{66}$ (from 2.66×10^{-5} Pa in Epi Suite down to 3.20×10^{-15} Pa in A-a) is clearly

238 seen in Figure 3. Epi Suite (U.S. Environmental Protection Agency) provides the highest vapour

239 pressures for all selected species in comparison with the rest of the data. Nannoolal et al. (2008)

240 and Myrdal-Yalkowsky (1997) data, both using the boiling point of Joback and Reid (1987),

241 provide similar results and present the lowest vapour pressures among the selected n-alkanes. For

242 the purpose of our sensitivity study, three representative datasets are nominated as an input,

243 namely Myrdal-Yalkowsky (1997) with the boiling point of Nannoolal et al. (2004, called B-c in

244 Figure 3 and hereafter), Compernolle et al. (2011, called Co) and Nannoolal et al. (2008) with the

245 boiling point of Joback and Reid (1987, called A-a). Hereafter we use the legend abbreviations in

246 Figure 3 when referring to these selected vapour pressures, which are towards the upper, mid- and

247 lower end of the reported data. The vapour pressure from the EPI Suite calculator has been

248 omitted from the analysis below because it has been considered in our previous study (Nikolova

249   et al., 2016).

250

251   The gas-phase concentration in the box is initialised with measured gas-phase concentrations in

252   the $C_{16}6H_{34}$-$C_{32}H_{66}$ range from a traffic site (Harrad et al., 2003) and reported in Table 6-S in the

253   Supplementary Information. All model simulations are run at 298 K; the effects of temperature on

254   vapour pressure differences as a function of carbon number are discussed in the Supplementary

255   Information.

256

257   We have performed a total of (17 modal compositions) x (5 σ values) x (3 non-volatile core

258   amounts) x (3 vapour pressures) = 765 model runs to explore the sensitivity of particle dynamics

259   on the neighbourhood scale.

260

261   The Supplementary Information contains information regarding the initial size distribution,

262   modal composition in the nucleation and Aitken modes, and gas-phase concentrations.

263   Accumulation-mode aerosol (particles diameter Dp > 100 nm) is not considered in this study.

264   Accumulation-mode particles have much smaller number concentrations than the nucleation and

265   Aitken modes in polluted urban areas, and are influenced by aging and transport over larger

266   scales.

267

268   **3.   RESULTS**

269   **3.1   Effect of composition on Nucleation-Mode Peak Diameter**

270   We consider first model runs in which the vapour pressure data follows Compernolle et al. (2011)

271   and nucleation mode particles initialised with 1% non-volatile material. The nucleation mode

272   peak diameter $D_{pg,nuc}$ is evaluated at 1 s and 100 s of model run-time in runs with varying modal

273   composition and composition standard deviations. Figure 4 shows $D_{pg,nuc}$ (y-axis) at 1s simulation

274   time, for each model run, plotted with respect to the modal composition and composition standard

Atmospheric
Chemistry
and Physics
Discussions

275   deviation, σ.

276

277   Figure 4 maps out the effect of nucleation-mode composition at this very early stage in the model

278   simulation. For example, at σ = 1 and initial mass distribution centred at $C_{20}H_{42}$ (purple solid line

279   with a square marker), the $D_{pg,nuc}$ decreased from 23 nm (initial diameter at t = 0 s) to 12 nm in

280   one second due to evaporation of volatile material from the particles. At σ = 2, $D_{pg,nuc}$ = 15 nm, a

281   somewhat larger diameter than for σ = 1, due to the inclusion of material of lesser volatility in the

282   particle composition and, hence, a decrease in evaporation overall. For modal compositions

283   between $C_{16}H_{34}$ and $C_{20}H_{44}$, an increase in σ leads to a pronounced deceleration in overall

284   evaporation and, hence, a much larger nucleation mode peak diameter at 1 s simulation time. The

285   opposite effect occurs for modal compositions of $C_{22}H_{46}$ and above, i.e. increasing σ for a given

286   modal composition decreases $D_{pg,nuc}$ at 1 s. This is due to the addition of quickly evaporating

287   lower molecular weight n-alkanes.

288

289   For a modal composition of $C_{21}H_{44}$, increasing σ makes almost no difference to the model

290   outcome at 1 s; below, we call the modal composition that shows insensitivity to σ for a given

291   model output time, the *threshold modal composition*. The model output time of 1 s corresponds to

292   the evaporation timescale of $C_{21}H_{44}$ under the current model setting, in analogy to the e-folding

293   time for an exponentially decaying process. That is, at this time, a significant proportion (e.g. $1-e^{-1}$

294    $\sim$ 63% for one e-folding time, and $1-e^{-2} \sim$ 86% for two e-folding times) of the initial mass has

295   been evaporated. Furthermore, the timescales are much shorter for those lower-carbon-number

296   compositions (e.g. $C_{20}H_{4,} C_{19}H_{40}, \ldots$) and much longer for those higher-carbon-number

297   compositions (e.g. $C_{22}H_{46}, C_{23}H_{48},\ldots$).

298

299   To continue the previous example of the modal composition of $C_{20}H_{42}$, the case with σ = 2

300   includes not only less volatile materials (i.e. higher-carbon-number SVOCs), but also an equal

301 amount of more volatile materials (i.e. lower-carbon-number SVOCs), as indicated by Figure 2.

302 One might suppose that inclusion of the more volatile material would balance the effect of

303 including less volatile materials. However, following our argument above, most of the lower-

304 carbon-number compounds including $C_{20}H_{42}$ will have evaporated before the given time of 1 s

305 due to their having much shorter evaporation timescales than $C_{21}H_{44}$. Thus any material

306 repartitioned from $C_{20}H_{42}$ to the lower-carbon-number compounds, in changing the model settings

307 from to $\sigma = 1$ to $\sigma = 2$, will not alter the total amount of evaporation and thus the shrinkage rate.

308

309 To take a second example: for $C_{22}H_{46}$, any material reallocated from $C_{22}H_{46}$ to the higher-carbon-

310 number compounds (due to changing the model setting from $\sigma = 1$ to $\sigma = 2$) will contribute

311 negligibly to the shrinkage simply because the evaporation timescales for those higher-carbon-

312 number components are much longer than 1 s, whilst the materials repartitioned from $C_{22}H_{46}$ to

313 the lower-carbon compounds will contribute significantly to evaporation in the first second of

314 model run-time, causing the decreasing trend of the curve shown in Figure 4.

315

316 One implication of this finding is that, if a timescale of 1 s is of interest, the aerosol dynamics of

317 the system is dominated by the threshold modal composition of $C_{21}H_{44}$. Those lower-carbon-

318 number compositions evaporate in less than 1 s and are approximately in equilibrium with their

319 respective gas concentrations in the environment. The higher-carbon-number compositions

320 evaporate slowly and at this time of 1 s, only a small or a negligible proportion has been

321 evaporated. A few compositions with highest carbon numbers (e.g. $C_{31}H_{64}$, $C_{32}H_{66}$) have

322 evaporated almost nothing. Therefore these compositions are effectively involatile for these

323 conditions.

324

325 Nucleation-mode particles have an initial non-volatile mass of 2.9 ng m^{-3}. Modal compositions

326 from $C_{16}H_{34}$ to $C_{19}H_{40}$ and $\sigma = 1$ will lose all their volatile mass in 1 s (Table 1). The initial $D_{pg,nuc}$

Atmospheric
Chemistry
and Physics
Discussions

327   decreases from 23 nm to 9 nm and no volatile material is present, i.e. particles are composed of

328   non-volatile core only. Little or no change is simulated in terms of mass and diameter for modal

329   composition $C_{32}H_{66}$.

330

331   At 100 s, the evaporation of existing mass from the surface of the particles is evident also for

332   higher molecular weight components (Table 1). The $D_{pg,nuc}$ at 100 s is plotted in Figure 5. The

333   diameter has further decreased with a more pronounced drop for all σ and modal compositions up

334   to $C_{25}H_{52}$. $C_{25}H_{52}$ is, therefore, the threshold modal composition at this model output time.

335

336   The horizontal line drawn at 10nm on Figure 5 corresponds to evaporation approximating

337   REPARTEE-like behaviour. At σ = 1, modal compositions in the range $C_{16}H_{34}$-$C_{23}H_{48}$ — and

338   vapour pressures and gas-phase partial pressures as detailed in the methodology — could

339   plausibly explain a particle diameter decrease from 23 nm to ~9 nm. Such a narrow range of

340   surrogate molecular compounds is incompatible with experimental observations such as Figure 1.

341   At σ = 2 and σ = 3, modal compositions from $C_{16}H_{34}$ up to $C_{22}H_{46}$ and $C_{21}H_{44}$, respectively, can

342   plausibly approximate REPARTEE-like behaviour. At σ = 4 and σ = 5 modal compositions from

343   $C_{16}H_{34}$ up to $C_{19}H_{40}$ and $C_{17}H_{36}$, respectively, plausibly simulate REPARTEE-like behaviour.

344

345   **3.2   Effect of Vapour Pressure on the Nucleation-Mode Peak Diameter**

346   We compare the simulated nucleation-mode peak diameter, $D_{pg,nuc}$, at 100 s using the vapour

347   pressure parameterisations B-c, Co and A-a (cf. Figure 3). The nucleation mode particles are

348   initialised with 1% non-volatile material in these simulations. $D_{pg,nuc}$ at 100 s using vapour

349   pressure parameterisations A-a and B-c (see Supplementary Information), shows the same general

350   behaviour as for vapour pressure parameterisation Co, but with a marked change in threshold

351   modal composition. In order of decreasing vapour pressure (Figure 3), the threshold modal

352   composition value changes from $C_{27}H_{56}$ for the B-c parameterisation (Figure 4-S in the

353 Supplementary Information), to $C_{25}H_{52}$ for Co (Figure 5), to $C_{22}H_{46}$ for A-a (Figure 5-S in the

354 Supplementary Information). We restrict ourselves to integer values of threshold modal

355 composition to maintain a straightforward connection back to the homologous chemical series in

356 Figure 1, although there is nothing in principle to prevent us from attributing real number values

357 to the threshold modal composition.

358

359 There is no composition with $\sigma = 4$ and $\sigma = 5$, at the lower volatility A-a vapour pressure

360 parameterisation, that produces REPARTEE-like behaviour; i.e., decrease of the nucleation-mode

361 peak diameter from 23 nm to 10 nm or below. At $\sigma = 5$, the nucleation-mode particles can lose a

362 maximum of ~9 nm of their initial diameter for modal composition $C_{16}H_{34}$ (please refer to Figure

363 5-S in the Supplementary Information). Little or no change in mode diameter is simulated for

364 modal compositions between $C_{24}H_{50}$ and $C_{32}H_{66}$ and $\sigma = 1$, indicating that these combinations of

365 composition and vapour pressure parameterisation are essentially involatile for the 100 s

366 simulation time. Modal compositions $C_{20}H_{42}$ ($\sigma = 1$), $C_{19}H_{40}$ ($\sigma = 2$) and $C_{17}H_{36}$ ($\sigma = 3$) can

367 produce REPARTEE-like aerosol dynamics.

368

369 Vapour pressure parameterisation B-c has the highest vapour pressure for all compounds in

370 comparison with Co and A-a. Hence, particles in the nucleation mode are subject to a more

371 pronounced evaporation, even for modal compositions $C_{28}H_{58}$ to $C_{32}H_{66}$. Nonetheless, only modal

372 compositions $C_{25}H_{52}$ ($\sigma = 1$), $C_{24}H_{50}$ ($\sigma = 2$), $C_{23}H_{48}$ ($\sigma = 3$), $C_{21}H_{44}$ ($\sigma = 4$) and $C_{20}H_{42}$ ($\sigma = 5$) are

373 able to produce the REPARTEE-like behaviour. Table 2 provides details on the modal

374 compositions and composition standard deviations that approximate the REPARTEE-like aerosol

375 dynamics for B-c, Co and A-a vapour pressure parameterisations.

376

377 The difference in 100-s $D_{pg,nuc}$ between the highest vapour pressure (B-c) and the lowest vapour

378 pressure (A-a) for all values of σ, is shown in Figure 6. The largest differences (10-14 nm)

29
30

15

Atmospheric
Chemistry
and Physics
Discussions

379   between the $D_{pg,nuc}$ occur for modal compositions between $C_{22}H_{46}$ and $C_{24}H_{50}$ and $\sigma = 1, 2, 3$. For

380   model run-time of 100 s, the variability of the UFP shrinkage due to the uncertainty of vapour

381   pressure data is highest for the compositions between $C_{22}H_{46}$ and $C_{24}H_{50}$. From Figure 3, we see

382   that the uncertainty of vapour pressure data increases monotonically with carbon number and is

383   highest for $C_{32}H_{66}$. However this high level of uncertainty for high-carbon compositions does not

384   exert a significant impact on the model results. We thus conclude that the accuracy of vapour

385   pressure values for very high or very low carbon compositions are not important for

386   neighbourhood-scale aerosol dynamics.

387

388   **3.3   Effect of Non-Volatile Core on the Nucleation Mode Peak Particle Diameter**

389   To consider how the fraction of involatile core interacts with the SVOCs composition and the

390   vapour pressure parameterisations, we define a '100-s effective involatile core': the nucleation

391   mode peak diameter at 100 s of evaporation. Figure 7 shows results for three non-volatile

392   fractions (initial1%, 5% and 10% based on mass) and vapour pressures A-a, B-c and Co (cf.

393   Figure 3), for a modal composition of $C_{16}H_{34}$. Results for the remaining modal compositions are

394   not plotted here because using modal composition $C_{16}H_{34}$ and an evaporation time of 100 s gives

395   the maximum reduction of the nucleation-mode peak diameter for all σ in our model runs.

396   However, we show the results for modal compositions $C_{24}H_{50}$ and $C_{32}H_{66}$ for completeness in the

397   Supplementary Information (Figure 7-S).

398

399   Because the mass-size distribution is held constant for each model initialisation (see

400   Supplementary Information), an increase of the non-volatile material in the nucleation mode

401   leads to a decrease in the total amount of n-alkane SVOC available for evaporation, and hence

402   leads to an increase in the nucleation mode 'dry' (i.e. involatile core only) diameter from ~9 nm

403   to ~12 nm. For the lowest volatility parameterisation (A-a), only the lightest surrogate

404   compounds near $C_{16}H_{34}$ are sufficiently volatile over the timescale of the model run to drive

405 evaporation of nucleation mode particles. As σ increases, an increasing number of lower volatility

406 components are added into the particle composition, causing the 100-s effective involatile core to

407 increase.

408

409 Considering REPARTEE-like behaviour, i.e., shrinkage of the nucleation mode diameter to ca. 10

410 nm, initial involatile core fractions of 5% or greater do not reproduce the observed behaviour.

411

412

413 **4.   DISCUSSION AND CONCLUSIONS**

414 The purpose of this study was to evaluate the importance of particle composition and saturation

415 vapour pressure on the evolution of urban ultrafine diesel particles on the neighbourhood scale

416 (<< 1 km) by means of numerical simulations. We present the effect of evaporation on the size-

417 resolved ultrafine particles and looked at the evolution of the nucleation-mode peak diameter

418 $D_{pg,nuc}$ depending on particle SVOC composition, vapour pressure, and fraction of involatile core

419 in the particles. We have used laboratory measurements of the size-resolved composition of the

420 ultrafine particles as an additional strong constraint on the plausibility of model parameter sets.

421 We identified a group of surrogate n-alkane compounds in the range $C_{16}H_{34}$-$C_{32}H_{66}$ that could

422 explain REPARTEE-like aerosol dynamics measured in London (Dall'Osto et al., 2011): i.e., a

423 final nucleation-mode peak diameter at 10 nm or below when particles were subject to

424 evaporation in a timescale of 100 s. Table 2 highlighted the set of parameters in terms of vapour

425 pressure and modal compositions that produce such REPARTEE-like behaviour.

426

427 Table 2 presents the sets of model parameters consistent with diameter reduction due to

428 evaporation. The question remains, however, to what extent these results are realistic and relevant

429 for the real-world atmosphere. Standard deviation σ = 1 for all vapour pressures narrows

430 significantly the contribution from the n-alkanes ([max(16, j-2):min(32, j+2)] for modal

Atmospheric
Chemistry
and Physics
Discussions

431 composition j), present in the initial composition of the nucleation mode particles. At σ = 2, the

432 main contributing compounds involved in particle composition are the modal composition j and

433 the surrogate molecules [max(16, j-4):min(32, j+4)]. This means that for the given vapour

434 pressure parameterisation, A-a, and modal composition $C_{19}H_{40}$, the compounds found in the

435 particles would be between $C_{15}H_{32}$ and $C_{23}H_{48.\setminus}$ However, $C_{16}H_{34}$ is the lower limit of surrogate

436 compounds in the model, so the Gaussian distribution of composition is truncated at the low-

437 carbon-number end in this case. At σ = 3, the contributing compounds found in the particles are

438 the surrogate molecules in the range [max(16, j-7):min(32, j+7)]. For a modal composition $C_{17}H_{36}$

439 and A-a vapour pressure, the range of participating compounds is $C_{16}H_{34}$-$C_{24}H_{50}$, similar to the

440 case of σ = 2. At σ = 4 and 5, the majority of the surrogate molecules in our range of n-alkanes

441 participate in the composition of particles, thus providing a reasonable range over the

442 contribution from diesel fuel and engine lubricating oil. The range at σ = 3 could be considered as

443 a transition range, while examples at σ = 2 would have compositions that are rather more limited

444 than available measurements in the Aitken mode (e.g. Figure 1), with a focus on the contribution

445 from the engine lubricating oil. Overall, narrow compositions would imply a strong gradient of

446 SVOCs across the nucleation and Aitken modes whereas broad compositions imply that SVOCs

447 are more or less evenly distributed across the ultrafine size range.

448

449 Table 3 shows an additionally constrained range of modal compositions consistent with what we

450 know from field and laboratory measurements combined. The lowest vapour pressure

451 parameterisations (A-a and the very similar B-a, see Figure 3) are less likely, at any modal

452 composition standard deviation (σ), to represent the laboratory and field observations together.

453 The results reported in Alam et al. (2016) and in Figure 1 show that diesel ultrafine particle

454 emissions are composed of a wealth of SVOCs that are mainly identified as straight and branched

455 alkanes in the range C_{11}-C_{33}, cycloalkanes (C_{11}-C_{25}), PAHs, various cyclic aromatics, alkyl

456 benzenes and decalins. They report emitted particulate size fractionated concentrations of n-

35
36

18

457 alkanes (cf. Figure 2-S in Supplementary Information) and point out that particles in the 5-100nm

458 diameter range consist mainly of high molecular weight SVOCs ($>C_{24}H_{50}$) associated with engine

459 lubricating oil.

460

461 Vapour pressure parameterisations used in this study and plotted in Figure 3, are one of the

462 crucial input parameters in assessing the rate at which condensation/evaporation can occur,

463 though they are poorly constrained. We introduced a new concept of threshold modal

464 composition, i.e. modal composition that is not sensitive to σ for a given model output time. In an

465 order of decreasing vapour pressure (Figure 3) and timescale of 100 s, the threshold modal

466 composition value changes from $C_{27}H_{56}$ for the B-c parameterisation (Figure 4-S, Supplementary

467 Information), to $C_{25}H_{52}$ for Co (Figure 5), to $C_{22}H_{46}$ for A-a (Figure 5-S, Supplementary

468 Information). Overall, the largest differences (~14 nm) in the 100-s $D_{pg,nuc}$ occur between the

469 highest (B-c) and the lowest (A-a) vapour pressure parameterisations for modal compositions

470 between $C_{22}H_{46}$ and $C_{24}H_{50}$ and composition standard deviation from 1 to 3. The vapour pressures

471 of components in this range are therefore critical for the modelling of nucleation-mode aerosol

472 dynamics on the neighbourhood scale. For components with volatility less than that for the $C_{22}H_{46}$

473 surrogate compound used here, all available vapour pressure parameterisations render these

474 compounds volatile over the 100-s timescale. These components will equilibrate with the gas

475 phase on these short timescales. Components with volatility greater than that of the $C_{24}H_{50}$

476 surrogate are effectively involatile over this timescale for all vapour pressure parameterisations,

477 and so will remain condensed and out-of-equilibrium with the gas phase on these timescales.

478

479 The other variable which will influence evaporation rate is the concentration of vapour

480 surrounding the particles. In this work, measured roadside vapour concentrations reported by

481 Harrad et al. (2003) are used (see also Nikolova et al., 2016). These represent an upper estimate

482 of gas-phase partial pressures away from roadside. Mixing of cleaner urban background air into

Atmospheric
Chemistry
and Physics
Discussions

483   the simulated air parcel would lower partial pressures and increase evaporation rates.

484

485   The 100-s effective involatile core (the nucleation mode peak diameter at 100 s of evaporation)

486   increased from ~9 nm to ~12 nm. This was attributed to the decrease in the total amount of n-

487   alkane surrogate compounds present for evaporation. As composition standard deviation σ

488   increased, an increasing number of lower volatility components added into the particle

489   composition caused the 100-s effective involatile core to further increase. Considering

490   REPARTEE-like behaviour, i.e., shrinkage of the nucleation mode diameter to ca. 10 nm, an

491   initial involatile core of 5% by mass or greater was not capable of reproducing the observed

492   behaviour in the atmosphere. Because the higher molecular weight (lower volatility) surrogate

493   molecules in the model are essentially involatile over the modelling timescale, the nucleation

494   mode dynamics due to SVOC is confounded with that due to the size of any involatile core

495   present in the particles.

496

497   Results (Figure 7) suggest that urban nucleation mode particles should be predominantly volatile

498   in order to produce REPARTEE-like behaviour. In these numerical experiments, the nature of the

499   non-volatile core need not be specified. This core could be composed of one or more low vapour

500   pressure compounds, not affected by condensation/evaporation on the timescale of the model and

501   measurements. On the other hand, as discussed in Nikolova et al. (2016), a non-volatile core

502   could be composed mainly of carbon and possibly some contribution from metal oxides and

503   sulphates. This difference in composition could be relevant to effects on human health. Li et al.

504   (2010) show that diesel truck emissions during idle induce a high level of oxidative stress in

505   human aortic endothelial cells, due to the type of metals and trace metals found in the exhaust,

506   while Xia et al. (2015) argue that traffic-related UFP act to promote airway inflammation due to

507   the rich content of organic species. The relative importance of these particles in affecting human

508   health merits further investigations.

Atmospheric
Chemistry
and Physics
Discussions

509

510   Laboratory exhaust diesel ultrafine particulate measurements are highly dependent on the

511   sampling methods. Measurements of the ultrafine particle composition from a diesel-fuelled

512   engine are still at an early stage and therefore more efforts should be put into developing

513   sampling protocols that target the composition of the nucleation and Aitken modes particles in a

514   realistic manner. There are no robust UFP chemical composition measurements at street scale and

515   therefore such measurements devoted to address in detail the composition of the traffic emitted

516   UFP in the atmosphere are urgently needed. Saturation vapour pressure is another source of large

517   uncertainties; our study lays out a strategy to determine which vapour pressures are most

518   significant in a given modelling scenario.

519

520

524

525

526

527

528

529

530

531

532

533

534

Atmospheric
Chemistry
and Physics
Discussions

535 **REFERENCES**

536

537 Alam, M. S, Rezaei, S. Z., Stark, C. P., Liang, Z., Xu, H. M. and Harrison, R. M.: The

538 characterisation of diesel exhaust particles – composition, size distribution and partitioning,

539 Faraday Discuss., 189, 69-84, 2016.

540

541 Alam, M. S., Liang, Z., Rezaei, S. Z., Stark, C. P., Xu, H. M., MacKenzie, A. R. and Harrison, R.

542 M.: Mapping and quantifying isomer sets of hydrocarbons ($\geq$C12) in diesel fuel, lubricating oil

543 and diesel exhaust samples using GC×GC-ToFMS, Atmos. Meas. Tech. Discuss., submitted,

544 2017.

545

546 Allen, L. R., Donahue, N. M., Shrivastava, M. K., Weitkamp, E. A., Sage, A. M., Grieshop, A. P.,

547 Lane, T. E., Pierce, J. R. and Pandis, S. N.: Rethinking organic aerosols: semivolatile emissions

548 and photochemical aging. Science, 315, 1259-62, 2007.

549

550 Atkinson, R. W., Fuller, G. W., Anderson, H. R., Harrison, R. M. and Armstrong, B.: Urban

551 ambient particle metrics and health: a time-series analysis, Epidemiology, 21, 501-511, 2010.

552

553 Biswas, S., Ntziachristos, L., Moore, K. F. and Sioutas, C: Particle volatility in the vicinity of a

554 freeway with heavy-duty diesel traffic, Atmos. Environ., 41, 3479-3493, 2007.

555

556 Chan, A. W. H., Isaacman, G., Wilson, K. R., Worton, D. R., Ruehl, C. R., Nah, T., Gentner, D.

557 R., Dallmann, T. R., Kirchstetter, T. W., Harley, R. A., Gilman, J. B., Kuster, W. C., de Gouw, J.

558 A., Offenberg, J. H., Kleindienst, T. E., Lin, Y. H., Rubitschun, C. L., Surratt, J. D., Hayes, P. L.,

559 Jimenez, J. L. and Goldstein, A. H.: Detailed chemical characterization of unresolved complex

560 mixtures in atmospheric organics:insights into emission sources, atmospheric processing, and

561   secondary organic aerosol formation, J. Geophys. Res.:Atmospheres, 118, 6783-6796, 2013.

562

563   Chickos, J. and Lipkind, D.: Hypothetical thermodynamic properties: vapour pressures and

564   vaporization enthalpies of the even n-Alkanes from C78 to C92 at T= 298.15K by correlation-gas

565   chromatography, J. Chem. Eng. Data, 53, 2432-2440, 2008.

566

567   Compernolle, S., Ceulemans, K. and Muller, J. -F.: Evaporation: a new vapour pressure

568   estimation method for organic molecules including non-additivity and intramolecular

569   interactions, Atmos. Chem. Phys., 11, 9431-9450, 2011.

570

571   Dall'Osto, M., Thorpe, A., Beddows, D.C.S., Harrison, R.M., Barlow, J.F., Dunbar, T., Williams,

572   P.I. and Coe, H.: Remarkable dynamics of nanoparticles in the urban atmosphere, Atmos. Chem.

573   Phys., 11, 6623-6637, 2011.

574

575   Harrad, S., Hassoun, S., Callen Romero, M.S. and Harrison, R.M.: Characterisation and source

576   attribution of the semi-volatile organic content of atmospheric particles and associate

577   vapour phase in Birmingham, UK, Atmos. Environ., 37, 4985-4991, 2003.

578

579   Harrison, R. M., Beddows, D. S. and Dall'Osto, M.: PMF analysis of wide-range particle size

580   spectra collected on a major highway, Environ. Sci. Technol., 45, 5522-5528, 2011.

581

582   Harrison, R. M., Dall'Osto, M., Beddows, D. C. S., Thorpe, A. J., Bloss, W. J., Allan, J. D., Coe,

583   H., Dorsey, J. R., Gallagher, M., Martin, C., Whitehead, J., Williams, P. I., Jones, R. L.,

584   Langridge, J. M., Benton, A. K., Ball, S. M., Langford, B., Hewitt, C. N., Davison, B., Martin,

585   D., Petersson, K. F., Henshaw, S. J., White, I. R., Shallcross, D. E., Barlow, J. F., Dunbar, T.,

586   Davies, F., Nemitz, E., Phillips, G. J., Helfter, C., Di Marco C. F. and Smith, S.: Atmospheric

587 chemistry and physics in the atmosphere of a developed megacity (London): an overview of the

588 REPARTEE experiment and its conclusions, Atmos. Chem. Phys., 12, 3065-3114, 2012.

589

590 Harrison, R.M., Jones, A.M., Beddows, D.C.S., Dall'Osto M. and Nikolova, I.:   Evaporation of

591 traffic-generated nanoparticles during advection from source, Atmos. Environ., 125, 1-7, 2016.

592

593 Joback, K. and Reid, R.: Estimation of Pure-component properties from group-contributions,

594 Chem. Eng. Commun., 57, 233-243, 1987.

595

596 Jacobson, M.Z.: Development and application of a new air pollution modeling system. 2. Aerosol

597 module structure and design, Atmos. Environ., 31, 131-144, 1997.

598

599 Julin, J., Winkler, P. M., Donahue, N. M., Wagner, P. E. and Riipinen, I.: Nera-unity mass

600 accomodation coefficient of organic molecules of varying structure, Environ. Sci. Technol., 48,

601 12083-12089, 2014.

602

603 Karnezi, E., Riipinen, I. and Pandis, S. N.: Measuring the atmospheric organic aerosol volatility

604 distribution: a theoretical analysis, Atmos. Meas. Tech. Discuss., 7, 2953-2965, 2014.

605

606 Kumar, P., Morawska, L., Birmili, W., Paasonen, P., Hu, M., Kulmala, M., Harrison, R. M.,

607 Norford, L. and Britter, R.: Ultrafine particles in cities, Environ. Intl., 66, 1-10, 2014.

608

609 Li, R., Ning, Z., Majumdar, R., Cui, J., Takabe, W., Jen, N., Sioutas, C. and Hsiai, T.: Ultrafine

610 particles from diesel vehicle emissions at different driving cycles induce differential vascular pro-

611 inflamatory responses: implications of chemical components and NF-kB signaling, Part. Fibre

612 Toxicol., 7-6, 2010.

613

614 Myrdal, P. B. and Yalkowsky, S. H.: Estimating pure component vapor pressures of complex

615 organic molecules, Ind. Eng. Chem. Res., 36, 2494-2499, 1997.

616

617 Nannoolal, Y., Rarey, J., Ramjugernath, D. and Cordes, W.: Estimation of pure component

618 properties: Part 1. Estimation of the normal boiling point of non-electrolyte organic compounds

619 via

620 group contributions and group interactions, Fluid Phase Equilibr., 226, 45-63, 2004.

621

622 Nannoolal, Y., Rarey, J. and Ramjugernath, D.: Estimation of pure component properties: Part 3.

623 Estimation of the vapor pressure of non-electrolyte organic compounds via group contributions

624 and group interactions, Fluid Phase Equilibr., 269, 117-133, 2008.

625

626 Nikolova, I., Janssen S., Vos, P., Vrancken, K., Mishra, V. and Berghmans, P.: Dispersion

627 modelling of traffic induced ultrafine particles in a street canyon in Antwerp, Belgium and

628 comparison with observations, Sci. Total Environ., 412-413, 336-43, 2011.

629

630 Nikolova, I., MacKenzie, A. R., Cai, X., Alam, M. S. and Harrison, R. M.: Modelling component

631 evaporation and coposition change of traffic-induced ultrafine particles during travel from street

632 canyon to urban background, Faraday Discuss.,189, 529-546, 2016.

633

634 Pugh, T. A. M., MacKenzie, A. R., Whyatt, J. D. and Hewitt, C. N.: Effectiveness of green

635 infrastructure for improvement of air quality in urban street canyons, Environ. Sci. Technol., 46,

636 7692-7699, 2012.

637

638 Robinson,. A. L., Donahue, N. M., Shrivastava, M. K., Weitkamp, E. A., Sage, A. M., Grieshop,

Atmospheric
Chemistry
and Physics
Discussions

639   A. P., Lane, T. E., Pierce, J. R. and Pandis, S. N.: Rethinking organic aerosols: semivolatile

640   emissions and photochemical aging, Science, 315, 1259-1262, 2007.

641

642   Ronkko, T., Lahde, T., Heikkila, J., Pirjola, L., Bauschke, U., Arnold, F., Schager, H., Rothe, D.,

643   Yli-Ojanpera, J. and Keskinen, J.: Effects of Gaseous Sulphuric Acid on Diesel Exhaust

644   Nanoparticle Formation and Characteristics, Environ. Sci. Technol., 47, 11882-11889, 2013.

645

646   Stein, S. E. and Brown, R. L.: Estimation of normal boiling points from group contributions, J.

647   Chem. Inf. Comp. Sci., 34, 581-58, 1994.

648

649   Topping, D., Barley, M., Bane, M. K., Higham, N., Aumont, B., Dingle, N., and McFiggans, G.:

650   UManSysProp v1.0: an online and open-source facility for molecular property prediction and

651   atmospheric aerosol calculations, Geosci. Model Dev.., 9, 899-914, 2016.

652

653   US EPA: Estimation Programs Interface Suite™ for Microsoft® Windows, v 4.11, United States

654   Environmental Protection Agency, Washington, DC, USA, 2017.

655

656   Wehner, B., Philippin, S., Wiedensohler, A., Scheer, V. and Vogt, R.: Variability of non-volatile

657   fractions of atmospheric aerosol particles with traffic influence, Atmos. Environ., 38, 6081-6090,

658   2004.

659

660   Xia, M., Viera-Hutchins, L., Garcia-Lloret, M., Rivas, M. N., Wise, P., McGhee, S. A., Chatila, Z.

661   K., Daher, N., Sioutas, C. and Chatila, T. A.: Vehicular exhaust particles promote allergic airway

662   inflammation through an aryl hydrocarbon receptor-notch signaling cascade, J. Allergy Clin.

663   Immun., 136, 441-453, 2015.

664

Atmospheric
Chemistry
and Physics
Discussions

665 **TABLE LEGENDS**

666 **Table 1.** Total mass M (ng m^{-3}) of nucleation mode peak particles at 1 s and 100 s of

667 simulation for modal compositions $C_{16}H_{34}$-$C_{32}H_{66}$ and composition standard

668 deviations, sigma. For comparison, the initial mass of the non-volatile material in the

669 nucleation mode peak particles is 2.9 ng m^{-3}.

670

671 **Table 2.** Modal composition ranges and composition standard deviations, sigma, producing

672 model results that approximate REPARTEE-like behaviour (see main text), for

673 different vapour pressure parameterisations. Initial involatile core in the nucleation

674 mode is set to 1%.

675

676 **Table 3.** Modal composition range and composition standard deviations, sigma, producing

677 more realistic results that approximate REPARTEE-like behaviour. Vapour pressure

678 parameterisation follows Myrdal and Yalkowski (1997; B-c in Figure 3),

679 Compernolle et al. (2011; Co in Figure 3), and Nannoolal 2008; A-a in Figure 3).

680 Column 'cn' indicates the carbon number of compounds n in the modal composition

681 with a contribution bigger than 1%.

682

683

684 **FIGURE LEGENDS**

685 **Figure 1.** A GC×GC chromatogram (contour plot) indicating homologous series of compounds

686 identified in diesel engine exhaust emissions. Emissions from a light-duty diesel

687 engine operating at 1800 revolutions per minute and 1.4 bar brake mean effective

688 pressure. Compounds identified in the contour plot are indicated by the coloured

689 polygons – Lower black polygons are n- + i-alkanes; red polygons are monocyclic

690 alkanes; green polygons are bicyclic alkanes; pink polygons are aldehydes + ketones;

Atmospheric
Chemistry
and Physics
Discussions

691   and upper black polygons are monocyclic aromatics. Each peak in the contour plot

692   represents a compound present in the emissions; warmer colours (e.g. red) are more

693   intense peaks while colder colours (blue) are smaller peaks. Contour plot were

694   produced by GC Image v2.5. Bar charts above show the volatility distribution of total

695   alkanes (red) and total identified species (black), indicating that the majority of the

696   emissions consist of alkanes. For details of the compound attribution method, see

697   Alam et al. (2017).

698

699 **Figure 2.** An example of nucleation mode UFP compositions, represented as mass fractions for

700   surrogate compounds $C_nH_{(2n+2)}$, n = [16:32], and described by a Gaussian distribution

701   centred on $C_{24}H_{50}$ with standard deviation, σ, from 1 to 5.

702

703 **Figure 3.** Vapour pressure data for selected n-alkanes $C_nH_{(2n+2)}$ where n =[16:32] at 298K.

704   Abbreviations in the legend point to the source as follows: A and B refer to the

705   vapour pressure data from Nannoolal et al. (2008) and Myrdal and Yalkowsky

706   (1997), respectively; -a, -b and -c refer to the boiling point of Joback and Reid

707   (1987), Stein and Brown (1994) and Nannoolal et al. (2004), respectively; ES refers

708   to Epi Suite calculator (U.S. Environmental Protection Agency); Co to Compernolle

709   et al. (2011); Ch to Chickos and Lipkind (2008).

710

711 **Figure 4.** Nucleation mode peak diameter Dp [nm] at 1 s of simulation depending on the modal

712   composition and the composition standard deviation. The initial nucleation mode

713   peak diameter is at 23nm (not shown on the figure).Vapour pressure data follows

714   Compernolle et al. (2011).

715

55

28

56

716 **Figure 5.** Nucleation mode peak diameter Dp [nm] at 100 s of simulation depending on the

717 modal composition and the composition standard deviation. The initial nucleation

718 mode peak diameter is at 23nm (not shown on the figure).Vapour pressure data

719 follows Compernolle et al. (2011).

720

721 **Figure 6.** $D_{pg,nuc}$ difference between the nucleation mode peak diameter (nm) when using B-c

722 vapour pressure and the nucleation mode peak diameter when using A-a vapour

723 pressure for modal compositions $C_nH_{(2n+2)}$ where n = [16:32].

724

725 **Figure 7.** Nucleation mode peak diameter Dp [nm] at 100 s: the '100-s effective involatile

726 core' for the nucleation mode. Results are shown at 1%, 5% and 10% initial non-

727 volatile material in the nucleation mode particles, modal composition $C_{16}H_{34}$ and for

728 various composition standard deviations.

729

730

731

732

733

734

735

736

737

738

739

740

741

Atmospheric
Chemistry
and Physics
Discussions

742

1s

Centre @ Sigma	$C_{16}H_{34}$	$C_{17}H_{36}$	$C_{18}H_{38}$	$C_{19}H_{40}$	$C_{20}H_{42}$	$C_{21}H_{44}$	$C_{22}H_{46}$	$C_{23}H_{48}$	$C_{24}H_{50}$	$C_{25}H_{52}$	$C_{26}H_{54}$	$C_{27}H_{56}$	$C_{28}H_{58}$	$C_{29}H_{60}$	$C_{30}H_{62}$	$C_{31}H_{64}$	$C_{32}H_{66}$
1	2.9	2.9	2.9	2.9	7.4	23.6	38.1	46.8	51.0	52.6	53.2	53.4	53.4	53.5	53.5	53.5	53.5
2	2.9	2.9	3.2	6.9	14.3	24.1	34.0	42.1	47.0	50.3	52.1	52.9	53.3	53.4	53.4	53.5	53.5
3	3.7	5.4	8.4	12.9	18.5	24.9	31.6	38.1	43.5	46.8	49.3	51.0	52.1	52.8	53.1	53.3	53.4
4	8.0	10.6	13.7	17.6	21.8	26.4	31.0	35.4	39.7	43.7	46.2	48.2	49.8	50.9	51.8	52.3	52.7
5	12.8	15.3	18.1	21.1	24.4	27.7	31.2	34.4	37.6	40.2	43.0	45.4	47.0	48.4	49.5	50.4	51.2

100s

Centre @ Sigma	$C_{16}H_{34}$	$C_{17}H_{36}$	$C_{18}H_{38}$	$C_{19}H_{40}$	$C_{20}H_{42}$	$C_{21}H_{44}$	$C_{22}H_{46}$	$C_{23}H_{48}$	$C_{24}H_{50}$	$C_{25}H_{52}$	$C_{26}H_{54}$	$C_{27}H_{56}$	$C_{28}H_{58}$	$C_{29}H_{60}$	$C_{30}H_{62}$	$C_{31}H_{64}$	$C_{32}H_{66}$
1	2.9	2.9	2.9	2.9	2.9	2.9	2.9	2.9	6.1	23.8	38.9	47.5	51.3	52.8	53.3	53.5	53.6
2	2.9	2.9	2.9	2.9	2.9	2.9	3.0	6.2	14.3	24.8	34.8	42.5	47.6	50.6	52.1	52.9	53.2
3	2.9	2.9	2.9	2.9	3.1	4.2	7.1	11.9	18.2	25.2	31.9	37.8	42.6	46.1	48.6	50.3	51.4
4	2.9	3.0	3.3	4.1	5.6	7.9	11.1	15.1	19.7	24.6	29.3	33.8	37.7	41.1	43.8	46.1	47.8
5	3.7	4.4	5.4	6.9	8.7	11.1	13.8	17.0	20.2	23.7	27.2	30.6	33.7	36.6	39.2	41.4	43.4

743
744
745
746
747
748
749
750

751 **Table 1.** Total mass M (ng m^{-3}) of nucleation mode peak particles at 1 s and 100 s of simulation

752 for modal compositions $C_{16}H_{34}$-$C_{32}H_{66}$ and composition standard deviations, sigma. For

753 comparison, the initial mass of the non-volatile material in the nucleation mode peak particles is

754 2.9 ng m^{-3}.

755
756
757
758
759
760
761
762
763
764
765
766
767

Atmospheric
Chemistry
and Physics

Open Access

Discussions

EGU

768

769

Vapour pressure Sigma	B-c	Co	A-a
1	<= $C_{25}H_{52}$	<= $C_{23}H_{48}$	<= $C_{20}H_{42}$
2	<= $C_{24}H_{50}$	<= $C_{22}H_{46}$	<= $C_{19}H_{40}$
3	<= $C_{23}H_{48}$	<= $C_{21}H_{44}$	<= $C_{17}H_{36}$
4	<= $C_{21}H_{44}$	<= $C_{19}H_{40}$	-
5	<= $C_{20}H_{42}$	<= $C_{17}H_{36}$	-

774

775 **Table 2.** Modal composition ranges and composition standard deviations, sigma, producing

776 model results that approximate REPARTEE-like behaviour (see main text), for different vapour

777 pressure parameterisations. Initial involatile core in the nucleation mode is set to 1%.

778

779

780

781

782

783

784

785

786

787

788

789

790

791

792

793

794

795

Vapour pressure Sigma	B-c	Co	A-a	cn -/+
1	-	-	-	2
2	$C_{21}H_{44}$-$C_{24}H_{50}$	$C_{21}H_{44}$-$C_{22}H_{46}$	-	4
3	$C_{19}H_{40}$-$C_{23}H_{48}$	$C_{19}H_{40}$-$C_{21}H_{44}$	-	7
4	$\leq C_{21}H_{44}$	$\leq C_{19}H_{40}$	-	9
5	$\leq C_{20}H_{42}$	$\leq C_{17}H_{36}$	-	11

800

801

Table 3. Modal composition range and composition standard deviations, sigma, producing more realistic results that approximate REPARTEE-like behaviour. Vapour pressure parameterisation follows Myrdal and Yalkowski (1997; B-c in Figure 3), Compernolle et al. (2011; Co in Figure 3), and Nannoolal et al., 2008; A-a in Figure 3). Column 'cn' indicates the carbon number of compounds n in the modal composition with a contribution bigger than 1%.

807

808
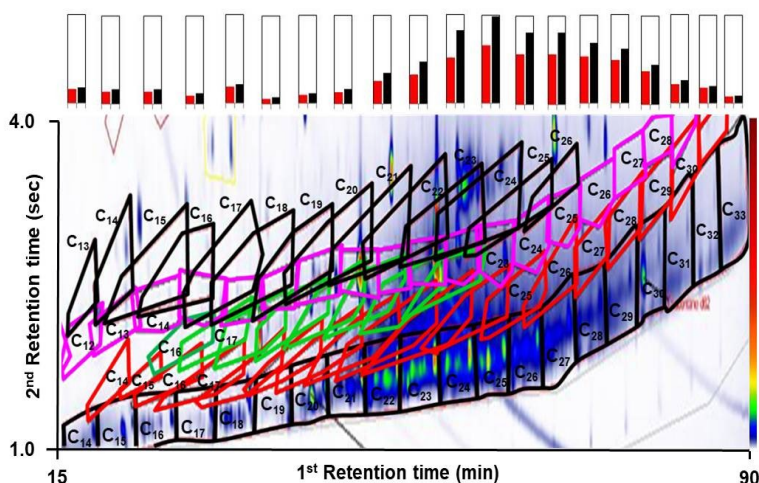
809

810

811

812

813

814

815

816

817

818

819

Atmospheric
Chemistry
and Physics
Discussions

Open Access

820

821

822

823

824

825

826

827

828

829

830

831

832   **Figure 1.** A GC×GC chromatogram (contour plot) indicating homologous series of compounds

833   identified in diesel engine exhaust emissions. Emissions from a light-duty diesel engine operating

834   at 1800 revolutions per minute and 1.4 bar brake mean effective pressure. Compounds identified

835   in the contour plot are indicated by the coloured polygons – Lower black polygons are n- + i-

836   alkanes; red polygons are monocyclic alkanes; green polygons are bicyclic alkanes; pink

837   polygons are aldehydes + ketones; and upper black polygons are monocyclic aromatics. Each

838   peak in the contour plot represents a compound present in the emissions; warmer colours (e.g.

839   red) are more intense peaks while colder colours (blue) are smaller peaks. Contour plot were

840   produced by GC Image v2.5. Bar charts above show the volatility distribution of total alkanes

841   (red) and total identified species (black), indicating that the majority of the emissions consist of

842   alkanes. For details of the compound attribution method, see Alam et al. (2017).

843

844

845

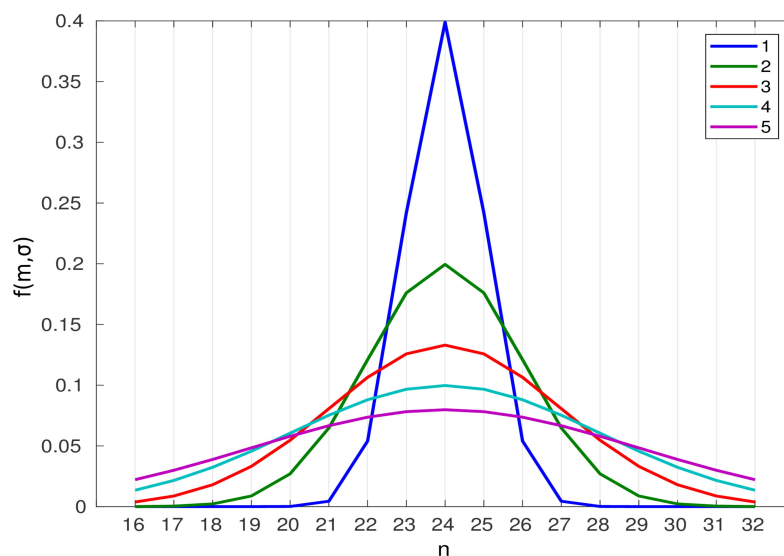Atmospheric Chemistry and Physics Discussions

Figure 2. An example of nucleation mode UFP compositions, represented as mass fractions for surrogate compounds $C_nH_{(2n+2)}$, n = [16:32], and described by a Gaussian distribution centred on $C_{24}H_{50}$ with standard deviation, σ, from 1 to 5.
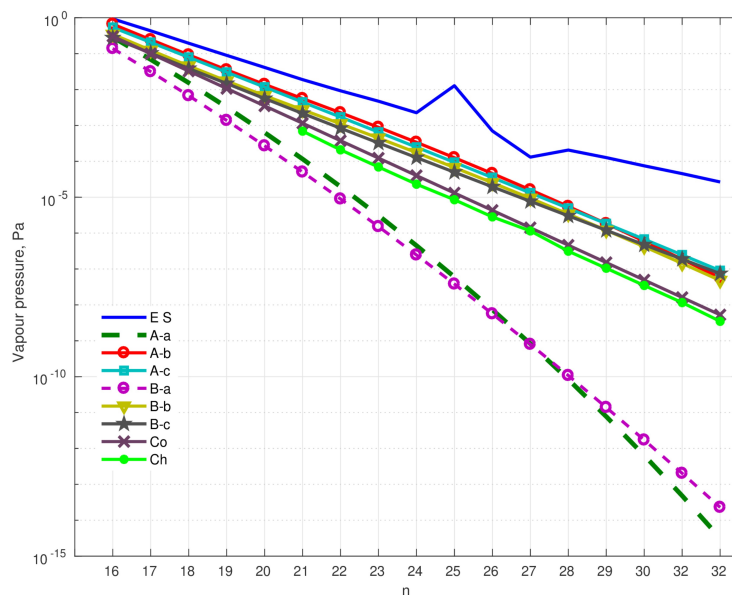
Atmospheric
Chemistry
and Physics
Discussions

872

873

874

885

Figure 3. Vapour pressure data for selected n-alkanes $C_nH_{(2n+2)}$ where n =[16:32] at 298K.

Abbreviations in the legend point to the source as follows: A and B refer to the vapour pressure

data from Nannoolal et al. (2008) and Myrdal and Yalkowsky (1997), respectively; -a, -b and -c

refer to the boiling point of Joback and Reid (1987), Stein and Brown (1994) and Nannoolal et al.

(2004), respectively; ES refers to Epi Suite calculator (U.S. Environmental Protection Agency);

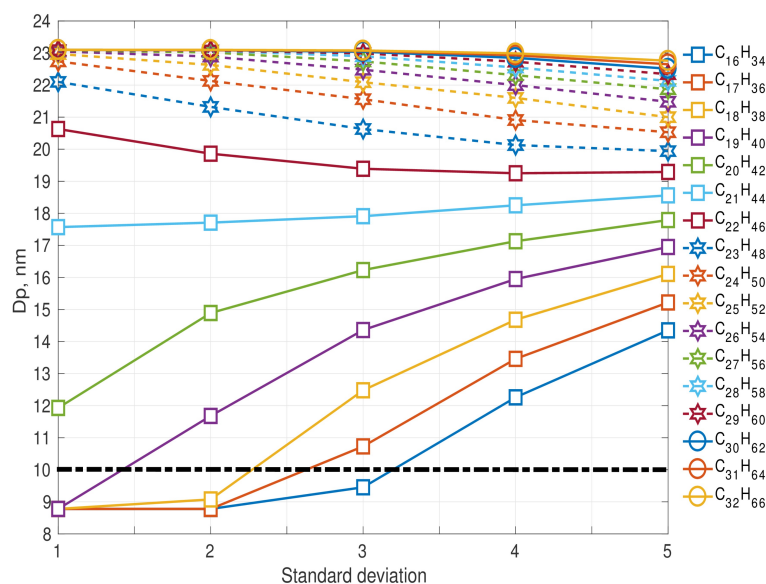Co to Compernolle et al. (2011); Ch to Chickos and Lipkind (2008).

892

893

894

895

896

897

898

899

900

901

902

903

904

905

906

907

908

909

910 **Figure 4.** Nucleation mode peak diameter Dp [nm] at 1 s of simulation depending on the modal

911 composition and the composition standard deviation. The initial nucleation mode peak diameter

912 is at 23nm (not shown on the figure).Vapour pressure data follows Compernolle et al. (2011).
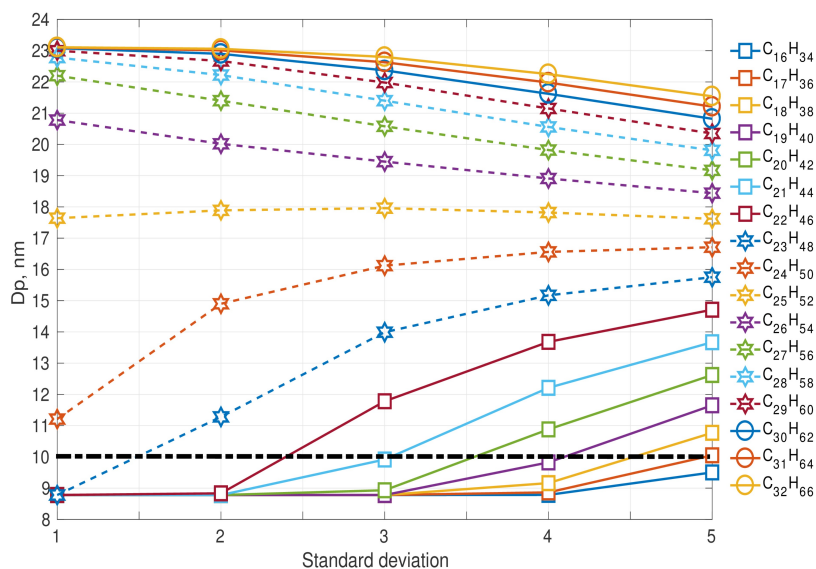
913

914

915

916

917

918

919

920

921

922

923

Figure 5. Nucleation mode peak diameter Dp [nm] at 100 s of simulation depending on the modal composition and the composition standard deviation. The initial nucleation mode peak diameter is at 23nm (not shown on the figure).Vapour pressure data follows Compernolle et al. (2011).
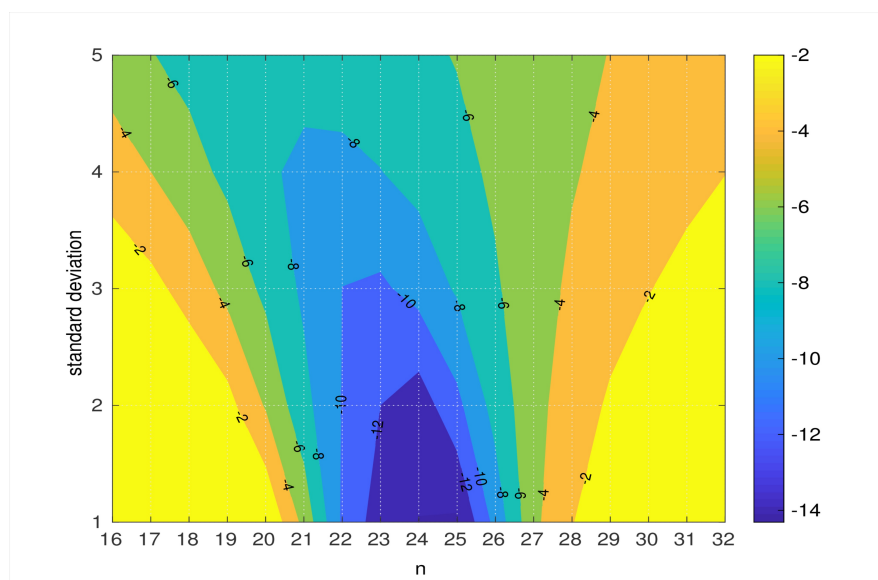
Figure 6. $D_{pg,nuc}$ difference between the nucleation mode peak diameter (nm) when using B-c

vapour pressure and the nucleation mode peak diameter when using A-a vapour pressure for
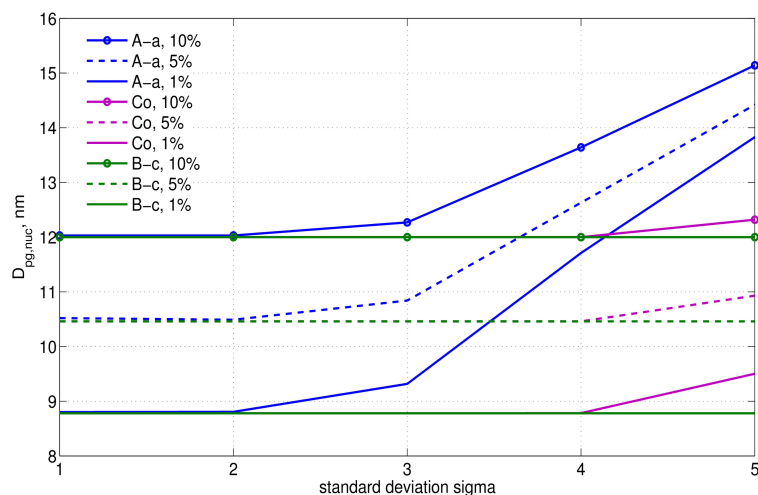
modal compositions $C_nH_{(2n+2)}$ where n = [16:32].

Atmospheric
Chemistry
and Physics
Discussions

976

977

978

979

980

981

982

983

984

985

986   **Figure 7.** Nucleation mode peak diameter Dp [nm] at 100 s: the '100-s effective involatile core'

987   for the nucleation mode. Results are shown at 1%, 5% and 10% initial non-volatile material in the

988   nucleation mode particles, modal composition $C_{16}H_{34}$ and for various composition standard

989   deviations.

990

991

992

993

994

995

996

997

998

999

1000